Scientific Reports

https://doi.org/10.1038/s41598-026-55336-9

Article in Press

A High-resolution metal–insulator–metal plasmonic biosensor with concentric ring resonators for carcinoembryonic antigen detection

Received: 8 April 2026

Accepted: 23 May 2026

Published online: 27 May 2026

Cite this article as: Bahador H., Izadiyar H. & Nilghaz A. A High-resolution metal–insulator–metal plasmonic biosensor with concentric ring resonators for carcinoembryonic antigen detection. *Sci Rep* (2026). https://doi.org/10.1038/s41598-026-55336-9

Hamid Bahador, Hadi Izadiyar & Azadeh Nilghaz

A High-Resolution Metal–Insulator–Metal Plasmonic Biosensor with Concentric Ring Resonators for Carcinoembryonic Antigen Detection

Hamid Bahador[1, *], Hadi Izadiyar[1], Azadeh Nilghaz[2]

[1] Department of Electrical and Computer Engineering, University of Mohaghegh Ardabili, Ardabil, Iran

[2] Drug Delivery, Disposition, and Dynamics, Monash University, Parkville, VIC 3052, Australia

*Corresponding author: hamid.bahador@uma.ac.ir

Abstract

High-resolution optical sensors are vital for detecting subtle refractive index variations associated with biomolecular interactions, such as changes in carcinoembryonic antigen (CEA) concentration. This work presents a compact metal–insulator–metal (MIM) plasmonic sensor with two concentric ring resonators, numerically investigated using finite-difference time-domain simulations. Structural parameters are optimized to maximize field confinement and resonant mode coupling, yielding a sensitivity of 1035 nm/RIU, a resonance linewidth of 3.75 nm, and a figure of merit of 276 RIU^{-1}. The sensor demonstrates precise spectral shifts corresponding to minute refractive index changes linked to CEA, while the influence of surface-bound layers and fabrication tolerances is also assessed to ensure robustness under practical conditions. These results highlight the sensor's potential as a high-resolution, label-free platform for monitoring CEA in biological samples.

Keyword: Metal–Insulator–Metal (MIM) plasmonic sensor, High-resolution refractive index sensing, Concentric ring resonator, Surface plasmon polaritons, Carcinoembryonic antigen (CEA) detection

Introduction

Recent advances in optical and photonic technologies have enabled the rapid creation of advanced devices capable of managing, guiding, and detecting light beams for a wide range of applications including communications, data processing, and sensing. Prominent examples of these achievements include

optical isolators [1], interferometers [2],plasmonic sensors [3], optical logic gates [4], and nanoantennas [5], all of which collectively attest to the diversity and growing penetration of modern photonic systems.

MIM plasmonic waveguide sensors are increasingly valued for their ability to confine electromagnetic fields at subwavelength scales, offering compact and highly sensitive platforms for refractive index sensing. Their strong light–matter interaction and compatibility with integrated photonic systems make them ideal for chemical, biological, and environmental detection. Accurate sensing depends not only on the magnitude of spectral shifts but also on the resolution and clarity of these shifts. High-resolution spectral features enable the detection of subtle environmental changes with greater precision and reduced uncertainty, making MIM sensors crucial for advancing precise plasmonic sensing technologies [6-8].

Surface Plasmon Resonance (SPR) has gained significant attention for its sensitivity and versatility in detecting small refractive index variations, arising from the interaction between incident light and free electrons at the metal-dielectric interface. SPR offers key benefits, including label-free, real-time detection, immunity to electromagnetic interference, and fast response times. Plasmonic sensors often use Metal-Insulator-Metal (MIM) or Insulator-Metal-Insulator (IMI) waveguides, coupled with cavity resonators for enhanced performance. MIM-based SPR systems are particularly effective due to their ability to confine electromagnetic fields, support a broad frequency range, and minimize bending losses, making them ideal for integrated photonic device development at the nanoscale [9, 10].

Early cancer diagnosis plays a decisive role in treatment success and patient survival, as initial disease stages often involve only subtle biochemical and optical changes in tissues or biological fluids. Detecting these small variations with high precision is essential for timely intervention and effective management. Advanced optical sensing platforms, particularly those capable of resolving closely spaced spectral features, enable reliable identification of early pathological changes with minimal sample preparation. [11, 12].

Biomarkers like alpha-fetoprotein (AFP) [13], prostate-specific antigen (PSA) [14], and carcinoembryonic antigen (CEA) are crucial in early cancer detection and monitoring [15, 16]. AFP is used for liver and testicular cancers but can also rise in non-cancerous conditions like hepatitis. PSA, linked to prostate cancer, may also be elevated in benign conditions such as benign prostatic hyperplasia (BPH). CEA, a broad-spectrum marker, is elevated in cancers such as colorectal, gastric, breast, and lung cancers, and its levels correlate with disease progression and metastasis. Early detection of CEA, especially in colorectal cancer, can significantly improve survival rates. CEA

levels below 2.5 ng/mL are considered normal, while levels between 2.5–5 ng/mL suggest possible malignancy, and levels above 5 ng/mL strongly indicate cancer [17-19]. Rapid, sensitive detection of these biomarkers, particularly CEA, is essential for accurate diagnosis and effective treatment management.

Khani and Hayati proposed an ultra-highly sensitive refractive index sensor employing an elliptical resonator coupled to a straight MIM waveguide through a silicon layer. The structure, analyzed using the finite-difference time-domain (FDTD) method, demonstrated multi-resonance behavior and achieved a sensitivity of 550 nm/RIU with a high figure of merit (FoM) of 282.5 RIU^{-1} around the resonance wavelength of 592 nm. The design benefits from a high-Q resonator and a strong field localization on the analyte, enabling ultra-sensitive detection[9]. In another study, Danaie and Shahzadi introduced a ring-shaped silicon nano-resonator embedded inside a circular cavity, acting as an optical notch filter with a Q-factor of 269. The sensor achieved a high sensitivity of 636 nm/RIU and a FoM of 211.3 RIU^{-1}. It was capable of detecting minute refractive index variations (±0.001), making it suitable for biomedical sensing. The structure's simplicity and high resolution further emphasize its applicability in integrated sensing systems [7].

Darabi and Malekshahi developed an optimized MIM filter for refractive index sensing with dual cut-off bands at 1008 nm and 1348 nm. The sensor achieved high sensitivity values of 7504 nm/RIU and 8000 nm/RIU for the two bands, with detection limits of 0.0039 RIU and 0.004 RIU. The figure of merit was 250.13 RIU^{-1} for the first band and 250 RIU^{-1} for the second [20]. Lotfi et al. presented a plasmonic sensor based on a double T-shaped resonator supporting Fano resonances. Their design utilized a conductor–insulator waveguide and achieved sensitivity enhancement by engineering narrowband and broadband mode interactions. Incorporating graphene at the core–cladding interface drastically increased sensitivity to 662.3 nm/RIU and yielded an extraordinary FoM of 6.6×10^5. The sensor was evaluated using samples with refractive indices in the range of 1.0–1.05 and was successfully applied to detect biomolecules in blood plasma [8]. Wang et al. developed an on-chip plasmonic sensor by integrating multiple rectangular resonators in an MIM waveguide system. The system exhibited multiple sharp Fano resonances by adjusting the relative distances between resonators, allowing a sensitivity of approximately 875 nm/RIU and an FoM of 1.861 $\times 10^4$. The extendable design and sharp spectral features make the structure highly suitable for biosensing, analytical chemistry, and photonic integrated circuits [21]. Similarly, Tasnim and Mohsin introduced a dual-mode SPR

biosensor based on a nanohole array in an MIM structure, utilizing silver (Ag) and titanium (Ti) layers. The device exhibited two sharp resonance peaks with sensitivities of 172 and 515 nm/RIU at 465 nm and 585 nm, respectively. Their analysis emphasized parameters such as transmission, reflection, FWHM, and Q-factor. The sensor was successfully applied to detect hemoglobin in blood and showed potential for sensing a variety of biomolecules including proteins, glucose, fructose, nucleic acids, and even whole cells [22]. A plasmonic metal-insulator-metal (MIM) nanosensor based on a five-Fano resonance structure is designed for label-free detection of viruses such as HSV, influenza, HIV, and bacteriophage M13, which offers a maximum sensitivity of 2372.1nm/RIU and a detection limit of 0.0328 at optimized geometric dimensions using the FDTD method. This nanosensor achieves a figure of merit (FOM) of 30.41 RIU^{-1} by coupling a rectangular waveguide with semi-ring and microring resonators [23]. Using a combination of a Y-shaped waveguide and two horizontal Fabry-Pré holes, Xingchun et al. have achieved a sensitivity of 1280 nm per refractive index unit (nm/RIU) and a figure of merit of 200 RIU-1, which offers optimal performance compared to many similar structures. These advances pave the way for the production of high-precision biological and chemical sensors at the nanometer scale [24]. In recent years, plasmonic sensors based on metal-insulator-metal (MIM) structures have attracted much attention in the field of cancer biomarker detection due to their ability to strongly confine light in subwavelength dimensions [cite: 1]. In this regard, Molaei-Yeznabad et al. designed and investigated a novel biosensor with a side-coupled semi-rectangular resonator for prostate-specific antigen (PSA) detection using the finite element method, which achieved a remarkable sensitivity of 1872.3 nm/RIU and a narrow half-maximum width of 24 nm by utilizing sharp Fano-type resonances. This structure, with a figure of merit (FOM) of 76.6 RIU^{-1}, a quality factor of 60.3, and a detection limit of 0.0108 RIU, shows much superior performance to similar designs such as dual ring resonators and, due to its simple geometry, has great potential for use in point-of-care detection equipment [25]. In this work, we present a detailed numerical investigation of the proposed plasmonic sensor using FDTD simulations. Key performance metrics, including sensitivity, resonance linewidth, quality factor, and estimated detection limit, are analyzed, along with the effects of surface-bound layers and fabrication tolerances, to evaluate the practical feasibility and potential applications of the sensor in chemical and molecular detection.

Numerical modeling and analysis method

The numerical simulations were performed using Lumerical FDTD Solutions. A non-uniform mesh was applied, with a minimum mesh size of 1 nm in regions with high field gradients near the resonator surface, and a coarser mesh in the surrounding regions to reduce computational cost. Perfectly Matched Layer (PML) boundary conditions were implemented in all directions to eliminate spurious reflections at the simulation boundaries. Silver was modeled using the experimental complex permittivity data of Johnson and Christy, accounting for frequency-dependent dispersion. The structure was excited using a broadband plane wave source polarized along the resonator axis, and the transmitted and reflected fields were collected using frequency-domain power monitors. Convergence was verified by refining the mesh until the resonance wavelength change was below 0.5 nm, ensuring accurate and reproducible results. A Transverse Magnetic (TM) polarized wave is launched at the input port to excite the fundamental TM plasmonic mode of the waveguide, in which the electric field possesses a component normal to the metal–dielectric interface. The excitation wavelength is swept from 700 nm to 1500 nm, ensuring efficient stimulation of surface plasmon polariton modes within the MIM waveguide and resulting in strong electromagnetic field confinement and pronounced resonant behavior. A uniform meshing scheme is employed throughout the computational domain, with mesh parameters carefully optimized to achieve a balance between numerical accuracy and computational efficiency.
For MIM waveguides employed in biosensing applications, analysis of the dispersion characteristics and effective refractive index of surface plasmon polaritons (SPPs) is essential. These hybrid electromagnetic modes are tightly confined to the metal–dielectric interfaces and are strongly influenced by the waveguide geometry and the optical properties of the constituent materials. The dispersion behavior and effective refractive index of the TM-polarized SPP mode directly govern phase propagation, field confinement, and resonance conditions, thereby playing a critical role in determining the sensing performance and resolution of the device.

The propagation characteristics of SPPs in a MIM waveguide are governed by the dispersion relation of the fundamental transverse magnetic (TM) mode, which is the only mode capable of supporting plasmonic confinement in MIM structures. The propagation constant β of SPPs is related to the effective refractive index n_{eff} by [22]:

$$\beta = k_0 n_{eff}, \quad k_0 = \frac{\omega}{c} \tag{1}$$

where ω is the angular frequency and c is the speed of light in vacuum. The effective refractive index is determined by the complex permittivities of the metal (ε_m) and dielectric (ε_d) layers and plays a critical role in defining phase velocity and sensing performance.

The electromagnetic field associated with TM-polarized SPP modes exhibits strong confinement at the metal–dielectric interfaces, with exponential decay away from the interface. The electric field distribution can be expressed as [26, 27]:

$$E(x,y,z) = E_0 e^{i(\beta x - \omega t)} e^{i(\beta z - \omega t)} \tag{2}$$

where *f(x,y)* represents the transverse field profile. The evanescent decay of the field is characterized by the decay constant κ, given by [26, 27]:

$$k = \sqrt{\beta^2 - k_0^2 e} \tag{3}$$

which depends on the operating wavelength and the permittivity of the surrounding media.

Sensor performance is evaluated using key metrics including sensitivity (S), full width at half maximum (FWHM), figure of merit (FoM), and quality factor (Q). Sensitivity is defined as [28]:

$$S = \frac{\Delta\lambda}{\Delta n} \ (\text{nm/RIU}) \tag{4}$$

where Δλ is the resonance wavelength shift induced by a refractive index change Δn. The spectral resolution of the sensor is described by FWHM of the resonance. Combining sensitivity and resolution, the FoM is given by [29]:

$$FoM = \frac{S}{FWHM} \ (\text{RIU}^{-1}) \tag{5}$$

while the quality factor is given by [29]:

$$Q = \frac{\lambda_{res}}{FWHM} \tag{6}$$

Structure and simulation

The proposed plasmonic sensor utilizes a MIM waveguide structure, incorporating two concentric ring resonators (CRRs) with narrow gaps. As shown in Figure 1, these resonators are symmetrically arranged on a silver layer with dimensions of 1500 × 1000 nm. For simulation purposes, a light source is used to excite SPPs within the waveguide. Silver is selected for its low optical loss and exceptional plasmonic properties in the visible and near-infrared regions, offering superior field confinement and quality factor compared to gold. The symmetrical placement of the CRRs induces strong resonant interactions and a uniform field distribution, contributing to enhanced sensitivity and performance. The sensor's dimensions have been optimized to maximize its efficiency for label-free biosensing applications. With an operational wavelength range spanning from 700 to 1500 nm, the sensor is capable of detecting minute refractive index variations induced by biomolecular interactions with high accuracy.

The geometric parameters defining the proposed plasmonic structure are illustrated in the two-dimensional schematic shown in Figure 1(b). These parameters include the ring radius, inter-resonator spacing, angular gap, waveguide–cavity separation, and waveguide dimensions, all of which play a critical role in determining the resonant behavior and sensing performance of the device. The optimal values of these design variables were obtained through systematic parametric analysis and are summarized in Table 1. This optimized configuration was employed in all subsequent simulations to ensure stable resonance characteristics and reliable sensing performance.

As shown in Table 2, the refractive index of the analyte varies with changes in the concentration of CEA in the solution. This relationship is described by the refractive index model $n=n_0+\Delta n$, where n_0 is the refractive index of water (taken as 1.33), and Δn represents the change in refractive index induced by the presence of CEA. The table provides the refractive index values corresponding to varying concentrations of CEA, ranging from 1 ng/ml to 5 ng/ml, highlighting the sensitivity of the sensor to small changes in CEA concentration. These variations in refractive index are crucial for the sensor's ability to detect and quantify the biomolecular interactions relevant to early-stage diagnostics.

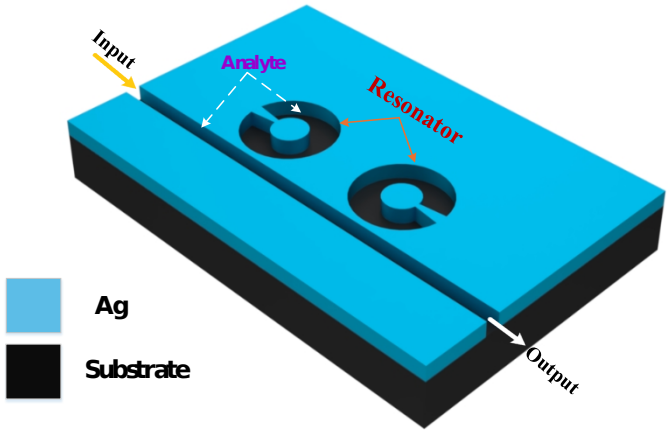

(a)

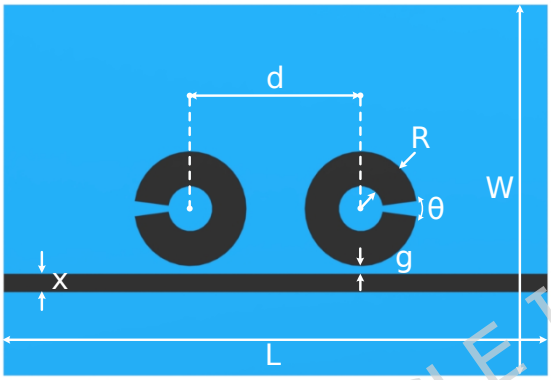

(b)

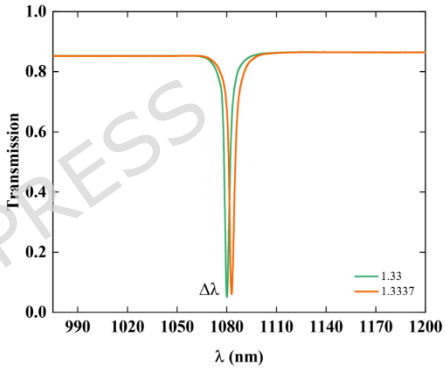

(c)

Figure 1: Schematic illustration of the metal-insulator-metal (MIM) sensor: (a) Three-dimensional representation of the sensor design, (b) Two-dimensional top view showing the structural parameters, (c)Transmittance characteristic of the proposed sensor with one resonant Mode.

Table 1: Key optimized parameters used in the simulation model

Name of the parameter	symbol	Value(nm)
Structure periodicity length	L	1500
Structure periodicity width	w	1000
the Radius ring	R	95
The distance between two resonators	d	470
the Angular gap of rings	θ	15
the gap between the waveguide and the cavity	g	10
the waveguide width	x	50
Structure thickness	h	100

Table 2: The refractive index of CEA with water (n_0=1.33)[30]

CEA concentration (ng/ml)	$n=n_0 + \Delta n$
1	1.3337
2	1.3374
3	1.3411
4	1.3448
5	1.3485

In practical biosensing applications, selective biorecognition is typically achieved by immobilizing receptor molecules (such as antibodies) on the resonator surface, particularly at locations with high field enhancement, to bind the target antigen (e.g., CEA). In our numerical model, we emulate this binding layer by placing a dielectric layer with a refractive index of 1.45 on the resonator surface, approximating the effect of a receptor-functionalized surface. While specific biorecognition mechanisms, surface functionalization models, or experimental validation are not included in this study, this approach allows us to investigate the resonance shift induced by surface-bound layers and estimate the potential sensitivity for biosensing applications.

The proposed side-coupled waveguide-excited configuration provides several practical advantages for biomarker sensing. First, it allows efficient excitation of the plasmonic resonator modes without requiring complex free-space optics. Second, the transmitted signal can be collected directly via the waveguide, reducing losses and simplifying detection. Third, this design is compatible with on-chip integration, facilitating compact and scalable biosensor arrays suitable for lab-on-chip or point-of-care applications. Finally, the guided-mode excitation reduces background scattering, which is particularly advantageous for low-concentration biomarker detection. These features make the side-coupled structure more practical and robust compared with conventional normal-incidence plasmonic biosensor platforms.

Fabrication process of the sensor

Although the present study is primarily based on numerical simulations, a fabrication-oriented discussion is included to demonstrate the practical feasibility of the proposed plasmonic sensor and to ensure that the simulated design remains compatible with realistic manufacturing constraints. In particular, an understanding of fabrication processes enables the incorporation of dimensional tolerances and structural imperfections into the simulation framework, thereby improving the reliability and applicability of the reported results.

Nanoimprint lithography (NIL) is a widely adopted, cost-effective technique for the fabrication of plasmonic nanostructures with high resolution and large-area uniformity [31]. In a typical NIL process, a thermoplastic polymer such as polymethyl methacrylate (PMMA) is spin-coated onto a silicon substrate and subsequently patterned using a pre-designed mold. A thin metallic layer, commonly silver or gold, is then deposited using electron-beam evaporation or physical vapor deposition techniques. Finally, the residual polymer layer is removed to define the intended plasmonic nanostructure [32]. Despite its advantages, NIL is subject to several fabrication-related challenges that can influence device performance. Non-uniform pressure during imprinting may lead to substrate deformation or incomplete pattern transfer, while misalignment between the mold and substrate can introduce geometric distortions [33]. Additionally, residual polymer layers formed at elevated processing temperatures may degrade the optical response of the sensor by altering effective cavity dimensions and coupling conditions [34]. Surface contamination and particulate defects can further compromise pattern fidelity. These effects can be mitigated through careful mold preparation, controlled imprint pressure, optimized processing temperatures, and stringent environmental cleanliness [35]. Consideration of these factors informs the simulation assumptions adopted in this work and supports the robustness of the proposed sensor design for future experimental realization.

To assess fabrication feasibility, we investigated the effect of dimensional deviations on the sensor response. Variations in key parameters, including the inner and outer ring radii, the inter-ring gap, and the waveguide-resonator coupling distance, were simulated within a range of ±5–10 nm, consistent with typical nanofabrication tolerances. The results (Figures 4–7) indicate that the resonance wavelength shifts only slightly and the Figure of Merit remains high, demonstrating that the sensor design is robust to realistic fabrication imperfections.

Results and Discussions

The observed narrow resonance originates from the coupling between the plasmonic modes of the dual-ring structure. The inner ring primarily supports a bright radiative mode, while the outer ring sustains a dark subradiant mode. The interference between these modes produces a Fano-like resonance, characterized by a sharp spectral dip with reduced radiative losses, resulting in a narrow linewidth. The strong field confinement near the resonator surface enhances interaction with any dielectric or functional layer placed on the surface, increasing sensitivity. Consequently, the Figure of Merit (FOM) is improved due to the combination of high

sensitivity and narrow spectral linewidth. The dual-ring geometry also provides tolerance to dimensional variations, as confirmed by the parametric studies in Figures 4–7, ensuring robust sensor performance.

The optimized geometrical parameters yielded a distinct resonance at 1080 nm, where a significant dip in transmission was observed. This transmission dip is attributed to the coupling between the resonant modes of the rings and the continuum modes, which results in an efficient energy transfer at the resonance wavelength.

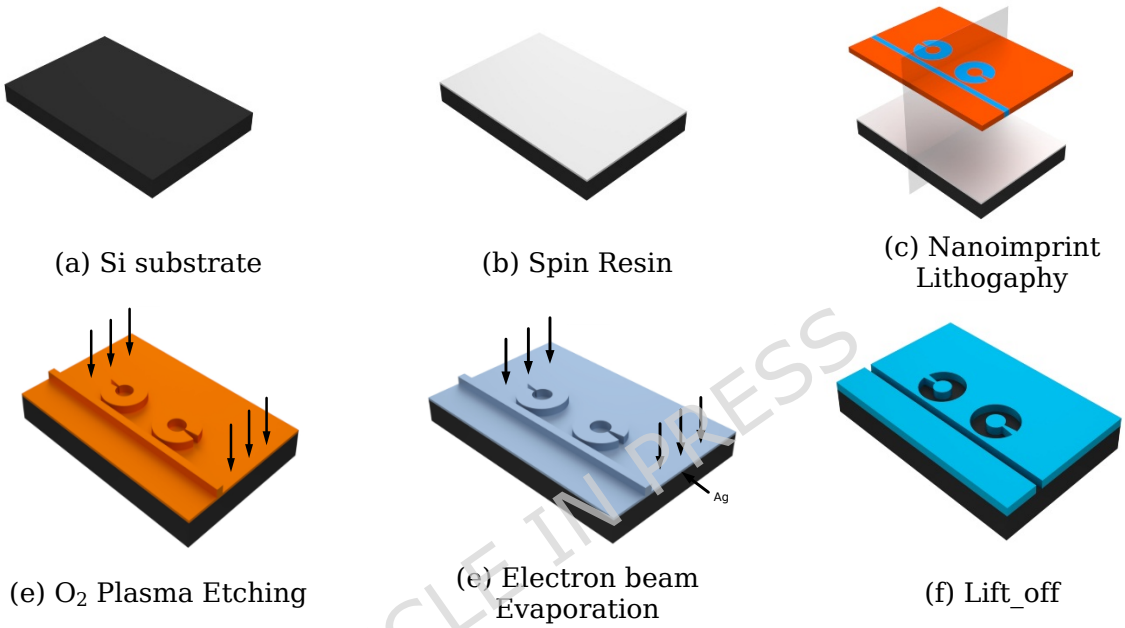

(a) Si substrate (b) Spin Resin (c) Nanoimprint Lithogaphy

(e) O_2 Plasma Etching (e) Electron beam Evaporation (f) Lift_off

Figure 2: Steps in manufacturing a biosensor, (a) Initial substrate, (b) First layer deposition, (c) Optical mask placement, (d) Second layer deposition, (e) Patterning and hole creation, (f) Gap creation and structure completion

Figure 3 illustrates the magnetic field intensity distribution in the central xz-plane of the sensor, showing two distinct conditions. In Figure 3a, at a non-resonant wavelength (λ = 1116 nm), the magnetic field is predominantly propagating through the waveguide, with minimal confinement or interaction within the resonators. This absence of resonance results in no significant light trapping or field enhancement. Conversely, Figure 3b illustrates the resonant condition at λ = 1080 nm, where the magnetic field is strongly confined within the ring resonators. At this wavelength, the incident light is effectively trapped due to the resonance between the incident wavelength and the resonant modes of the rings, leading to a sharp drop in transmission. This phenomenon reflects the efficient energy localization within the resonators, confirming the ability of the structure to filter and trap light at specific wavelengths.

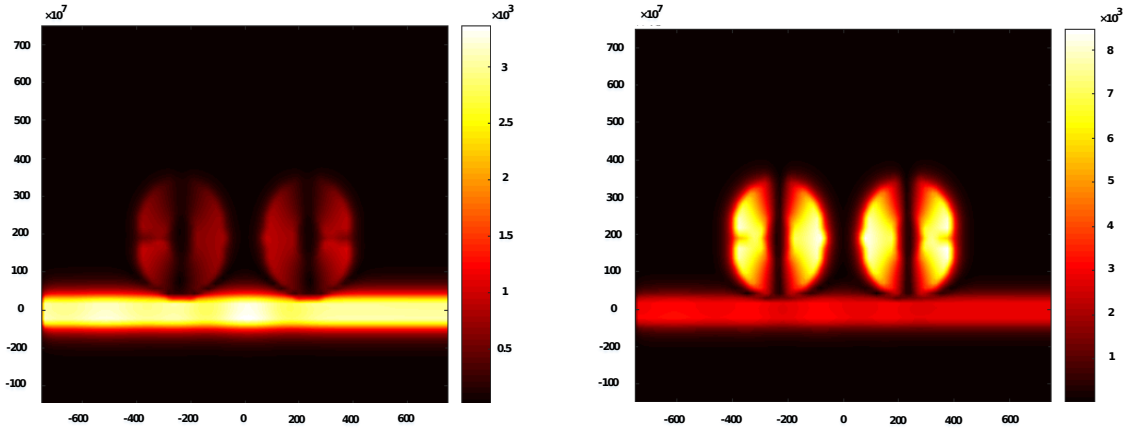

(a) (b)

Figure 3: Magnetic field intensity distribution ($|H|^2$) in the central xz-plane of the designed MIM biosensor: (a) At λ = 1116 nm, where no resonance occurs and the incident field mainly propagates through the waveguide without significant confinement b) At λ =1080 nm, where a strong resonance mode is excited and the magnetic field is effectively confined within the resonator.

Achieving high performance in refractive index sensors requires optimizing sensitivity (S), enhancing the FoM, and minimizing the FWHM. The sensor's efficiency is significantly influenced by several structural parameters, including the coupling gap between the waveguide and the resonators (g), the radius of the concentric ring resonators (R), the angular gap within the resonators (θ), and the spacing between the concentric rings (d). Fine-tuning these geometric factors can substantially improve the sensor's sensing capabilities, making the proposed biosensor particularly effective for a wide range of biomolecular detection applications.

To identify the optimal radius (R) for the side-coupled concentric ring resonator (Figure 4(a)), a systematic parametric analysis was performed. In this procedure, the radius was varied from 80 nm to 110 nm in 5 nm increments. The resulting variation in the FoM, shown in Figure 4(b), reveals a strong dependence of the FoM on the resonator radius, underscoring the importance of precise geometric tuning in plasmonic biosensor design.

For smaller radii (R ~ 80 nm), the FoM remains relatively low. This behavior is attributed to insufficient plasmonic mode confinement within the ring resonator, leading to weak light–matter interactions and suboptimal coupling to the MIM waveguide. As the radius increases, the FoM improves significantly, peaking at R = 95 nm, where optimal electromagnetic field confinement and phase matching between the waveguide mode and the resonant mode of the ring are achieved. At this optimal radius, the sensor exhibits a balance between enhanced field confinement and minimal radiative losses, resulting in a sharp, deep resonance dip in the transmission spectrum, a hallmark of high-sensitivity sensing performance.

Beyond this optimal radius, increasing the resonator size leads to a gradual reduction in the FoM. For radii greater than 95 nm, the FoM decreases due to

weaker field localization, increased radiation leakage, and reduced coupling efficiency between the waveguide and resonator. These effects result in a broader resonance linewidth, which reduces both the FoM and the sensor's resolution.

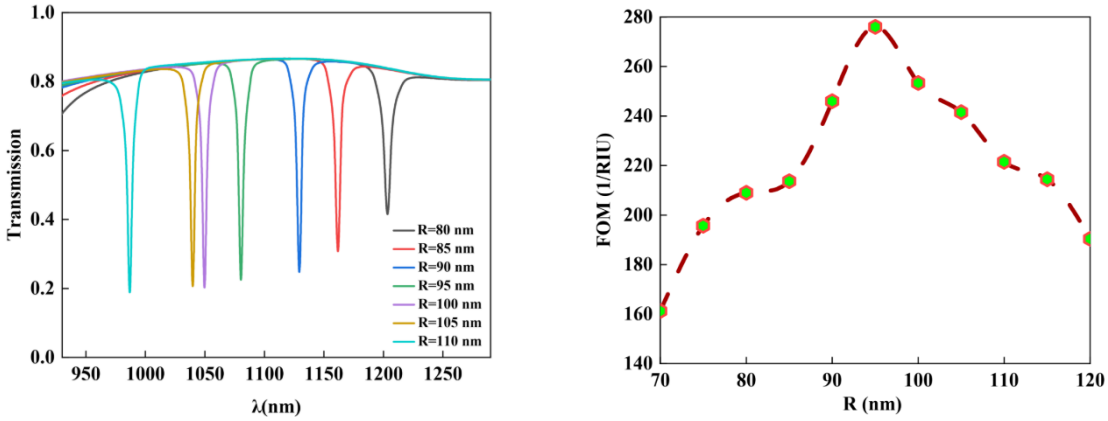

(a) (b)

Figure 4: (a) Variation of the Transmission spectrum and, (b) the FOM value with respect to the concentric ring radius

Figure 5(a) illustrates the evolution of the transmission spectrum of the MIM-based plasmonic sensor as the coupling gap between the waveguide and the ring resonator is varied from 7 nm to 13 nm. A progressive increase in the gap distance leads to a noticeable reduction in the resonance depth, reflecting a gradual weakening of the evanescent coupling between the guided mode and the resonant cavity. In addition, a slight blue shift of the resonance wavelength and a modest broadening of the resonance linewidth are observed as the gap increases. These effects indicate that the gap distance plays a critical role in governing near-field interaction strength, radiative losses, and energy exchange efficiency within the sensing structure.

A gap size of g = 10 nm yields the most favorable sensing performance among the investigated values. As shown in Figure 5(b), this configuration provides the FoM and spectral amplitude by establishing an optimal coupling regime. At this gap, sufficient electromagnetic energy is transferred into the resonator to produce a pronounced resonance while preserving a narrow linewidth through controlled leakage. The resulting combination of strong field localization and sharp spectral response is particularly advantageous for high-resolution biosensing applications, where low detection limits and precise refractive index discrimination are required.

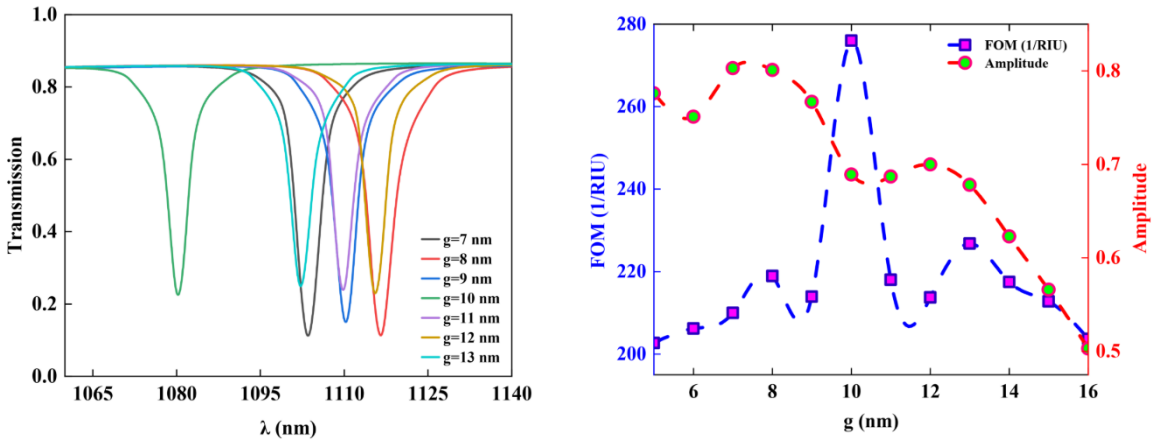

(a) (b)

Figure 5: (a) Variation of the Transmission spectrum and, (b) the FOM and amplitude values with respect to the gap between the concentric rings

Figure 6(a) presents the transmission response of the plasmonic sensor for different values of the angular gap (θ) of the ring resonator, varied from 9° to 21° in increments of 2°. Both the resonance wavelength and the depth of the transmission minimum exhibit pronounced sensitivity to this parameter. As θ increases, a gradual blue shift of the resonance is observed, which can be attributed to the effective shortening of the optical path within the resonator and the consequent modification of the phase-matching condition required for resonance excitation. Concurrently, the resonance depth increases up to an intermediate angle and then diminishes for larger values of θ, reflecting the interplay between coupling efficiency and radiation-induced losses.

An angular gap of θ = 15° provides the most favorable sensing characteristics among the examined configurations. As illustrated in Figure 6(b), this geometry produces a well-defined and spectrally narrow resonance with a steep transmission slope, indicative of strong electromagnetic field localization in the gap region and an enhanced quality factor. The resulting improvement in both sensitivity and figure of merit highlights the importance of angular gap optimization for achieving high-resolution sensing. At this angle, efficient mode excitation is achieved without excessive radiative leakage, establishing a balanced operating regime that is well suited for precise refractive index detection in biosensing applications.

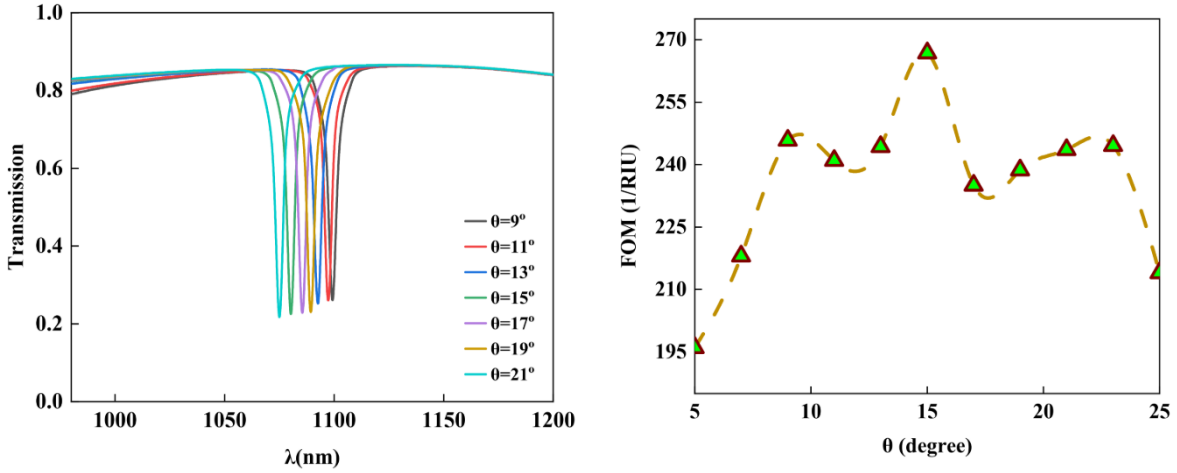

(a) (b)

Figure 6: (a) Variation of the Transmission spectrum and, (b) the FOM values with respect to the concentric ring gap angle

Figure 7(a) depicts the transmission response of the plasmonic sensor as the center-to-center separation between the two ring resonators (d) is varied from 440 nm to 500 nm in 10 nm increments. Variations in this parameter lead to noticeable changes in both the spectral position and the profile of the resonance. As the inter-ring distance increases, the resonance wavelength undergoes a gradual red shift, which can be attributed to the elongation of the effective optical path and the modified plasmonic coupling dynamics between the two resonators. In addition, the resonance depth and linewidth exhibit a non-monotonic trend, reflecting the competing influences of inter-resonator coupling strength and radiation-related losses.

An optimal sensing performance is achieved at an inter-ring distance of d = 470 nm, where the transmission spectrum displays the most pronounced and spectrally narrow resonance feature. This configuration corresponds to enhanced electromagnetic field localization in the coupling region and a maximized quality factor. As shown in Figure 7(b), these characteristics lead to the highest sensitivity and figure of merit among the examined cases. At this separation, the coupling between the resonators is sufficiently strong to support efficient energy exchange while remaining weak enough to suppress excessive radiative leakage. Deviations from this distance, either toward smaller or larger values, result

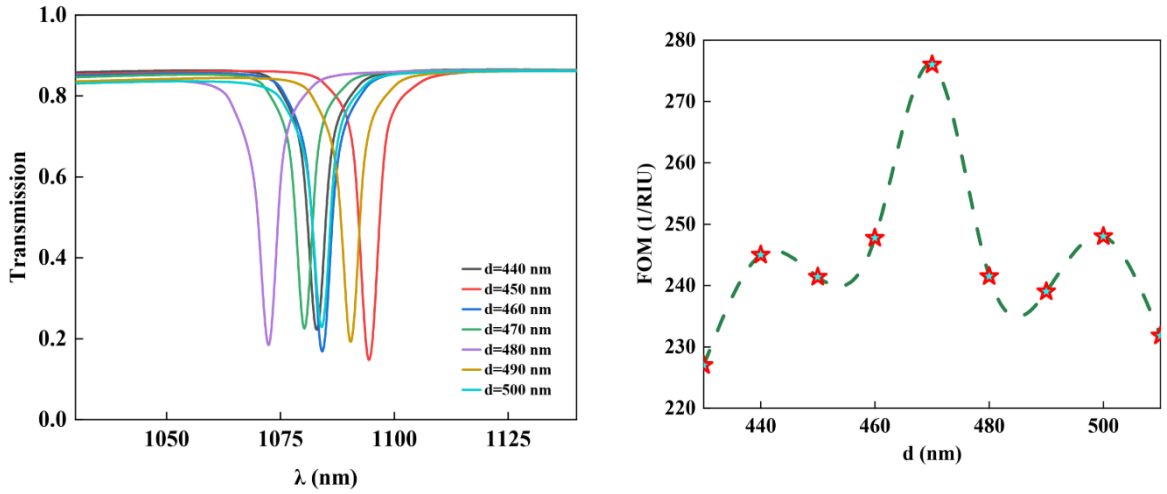

(a) (b)

Figure 7: Variation of the Transmission spectrum and, (b) the FOM values with respect to the inter-ring spacing

in over coupling or under coupling, respectively, both of which degrade the resonance quality and overall sensor performance. Consequently, the inter-ring spacing of 470 nm is selected as the optimal geometry for achieving high-resolution refractive index sensing in biosensing applications.

Following geometric optimization, the sensing performance of the proposed structure was quantitatively assessed using a reference analyte with a refractive index of 1.33. Variations in analyte concentration were modeled through incremental changes in refractive index (Δn), and the corresponding spectral response was analyzed. As illustrated in Figure 8, systematic shifts in the resonance wavelength are observed with increasing refractive index, confirming the strong dependence of the transmission characteristics on the surrounding medium. From these measurements, a sensitivity of 1035 nm/RIU, a FWHM of 3.75 nm, and a FoM of 276 RIU^{-1} were extracted.

To further characterize the sensor's performance, the detection limit (DL) can be estimated from the simulated resonance linewidth ($\Delta\lambda$=3.75 nm) and sensitivity (S=1035 nm/RIU). Assuming that wavelength shifts as small as 1/10 of the linewidth can be reliably resolved under ideal conditions, the detection limit is calculated as DL≈3.6×10^{-4} RIU. This estimate indicates that the proposed dual-ring plasmonic sensor has the potential to detect very small refractive index changes. It should be noted that in practical experimental setups, the actual detection limit will depend on factors such as spectral resolution, measurement noise, and surface functionalization quality.

The sensor demonstrates pronounced responsiveness within the refractive index range of 1.3337–1.3485, as summarized in Table 3, which correlates the refractive index variation of the analyte with changes in CEA concentration. This operating range is particularly relevant for biosensing applications, where low biomarker concentrations typically induce only subtle refractive index shifts. The narrow

resonance linewidth and high figure of merit confirm the high-resolution capability of the proposed structure, enabling accurate tracking of CEA-induced refractive index changes. Such precision is essential for early cancer diagnosis and longitudinal monitoring, where weak biomolecular signatures must be reliably distinguished from background noise.

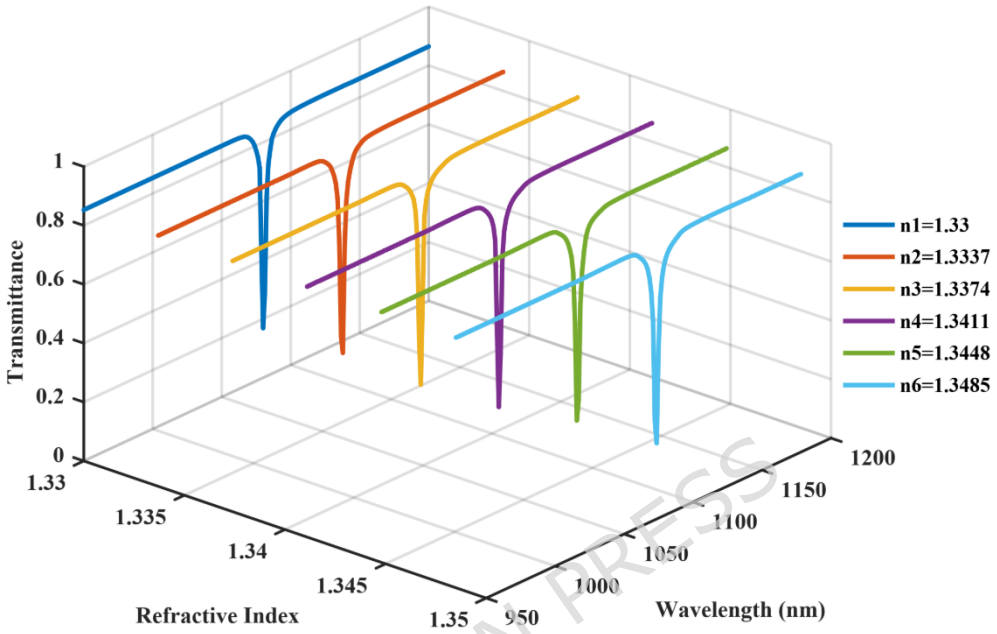

Figure 8: 3D transmittance spectra of the designed sensor plotted against wavelength and ambient refractive index (n = 1.33–1.3485). A distinct redshift of the resonance dip is observed as the refractive index increases, confirming the sensor's high sensitivity.

While some previously reported plasmonic sensors exhibit higher absolute sensitivity values, the present dual-ring design achieves a favorable combination of sensitivity, narrow resonance linewidth, and fabrication tolerance, resulting in a high Figure of Merit (FOM). Therefore, the proposed sensor should be considered competitive rather than strictly superior. Table 3 summarizes a comparison with recent studies, showing that our design maintains robust performance under structural variations and strong field confinement near the surface, which are critical for practical biosensing applications.

Table 3: Comparison of the sensing performance of the proposed biosensor with previously reported

Topology	Max sensitivity(nm/RIU)	Max FOM(1/RIU)	References

Elliptical resonator coupled Si ring resonator	550	282.3	[9]
Semi-ring arc	636	211.3	[7]
Y-shaped MIM plasmonic	2372.1	30.41	[23]
H-shaped resonator	1280	200	[24]
L-shaped MIM resonator	1960	118.25	[36]
Tapered WG	1638	21.84	[37]
Coupled semi-rectangular	1132.14	48.17	[38]
Semi-elliptical WG cavity	1872.3	76.6	[25]
Octagonal resonator	1384	28.4	[39]
This work	2197.76	58.126	[40]
	1035	276	-

Conclusion

A high-resolution plasmonic sensor based on a MIM waveguide coupled with two concentric ring resonators has been systematically analyzed through numerical simulations. Geometric optimization and electromagnetic modeling reveal strong field confinement and sharply defined resonance features, producing a sensitivity of 1035 nm/RIU, a resonance linewidth of 3.75 nm, and a figure of merit of 276 RIU^{-1}. The sensor exhibits a clear and monotonic response to small refractive index variations corresponding to CEA concentrations, demonstrating its potential for precise, label-free biomarker detection. Surface-bound layers and realistic fabrication tolerances are considered, confirming the robustness of the design. Overall, these findings establish the proposed structure as a compact and reliable platform for high-resolution monitoring of CEA, providing a strong foundation for potential experimental realization in biosensing applications.

Declarations

Data Availability

The data that support the findings of this study are available from the corresponding author upon reasonable request.

Competing Interests

The authors declare no competing interests.

Funding

No funding was received for conducting this research.

Author Contributions:

Hamid Bahador: Conceptualization, Methodology, Software, Validation, Formal analysis, Investigation, Data curation, Resources, Writing – review & editing, Visualization;

Hadi Izadiyar: Methodology, Investigation, Resources, Writing – original draft preparation.

Azadeh Nilghaz: Supervision, Software, Validation, Writing – review & editing.

All authors have read and approved the final manuscript.

References

1 .Rahad, R., et al., A novel plasmonic MIM sensor using integrated 1× 2 demultiplexer for individual lab-on-chip detection of human blood group and diabetes level in the visible to near-infrared region. IEEE Sensors Journal, 2024. **24**(8): p. 12034-12041.

2 .Butt, M.A., M. Shahbaz, and R. Piramidowicz. Racetrack ring resonator integrated with multimode interferometer structure based on low-cost silica–titania platform for refractive index sensing application. in Photonics. 2023. MDPI.

3 .Rahad, R., et al ,.Plasmonic refractive index sensing in the early diagnosis of diabetes, anemia, and cancer: an exploration of biological biomarkers. Results in Physics, 2023. **49**: p. 106478.

4 .Al-Musawi, H.K., et al., Plasmonic logic gates based on dielectric-metal-dielectric design with two optical communication bands. Optik, 2020. **223**: p. 165416.

5 .Rahad, R., et al., Graphene-metamaterial based tunable broadband polarization insensitive absorber for terahertz antenna design. Ieee Access, 2024. **12**: p. 48654-48667.

6 .Butt, M.A.J.P., Review of innovative cavity designs in metal–insulator-metal waveguide-based plasmonic sensors. 2025. **20**(6): p. 4257-4276.

7 .Danaie, M. and A. Shahzadi, Design of a high-resolution metal–insulator–metal plasmonic refractive index sensor based on a ring-shaped Si resonator. Plasmonics, 2019. **14**(6): p. 1453-1465.

8 .Lotfi, F., N. Sang-Nourpour, and R. Kheradmand, Resonator-based nanoscale plasmonic sensor made of metal–graphene–insulator interfaces. Results in Physics, 2024. **64**: p. 107922.

9 .Khani, S. and M. Hayati, An ultra-high sensitive plasmonic refractive index sensor using an elliptical resonator and MIM waveguide. Superlattices and microstructures, 2021. **156**: p. 106970.

10 .Rahad, R., M.A. Hossain, and N. Hossain, Numerical analysis utilizing a MIM plasmonic sensor for the detection of various bacteria. Plasmonics, 2025. **20**(6): p. 3583-3592.

11 .Fitzgerald, R.C., et al., The future of early cancer detection. Nature medicine, 2022. **28**(4): p. 666-677.

12 .Tai, W., et al., based sensors for visual detection of alkaline phosphatase and alpha-fetoprotein via the distance readout. Sensors and Actuators B: Chemical, 2023. **384**: p. 133666.

13 .Wang, R., Q. Wang, and P. Li, Significance of carcinoembryonic antigen detection in the early diagnosis of colorectal cancer: A systematic review and meta-analysis. World Journal of Gastrointestinal Surgery, 2023. **15**(12): p. 2907.

14 .Kiio, L.K., et al., Ultrasensitive immunosensor for multiplex detection of cancer biomarkers carcinoembryonic antigen (CEA) and yamaguchi sarcoma viral oncogene homolog 1 (YES1) based on eco-friendly synthesized gold nanoparticles. Talanta, 2024. **266**: p. 124934.
15 .Babazad, M.A., et al., Recent progress and challenges in biosensing of carcinoembryonic antigen. TrAC Trends in Analytical Chemistry, 2024. **180**: p. 117964.
16 .Hasan, D., Diagnostic impact of CEA and CA 15-3 on chemotherapy monitoring of breast cancer patients. Journal of Circulating Biomarkers, 2022. **11**: p. 57.
17 .Hariri, M., et al., Biosensor-based nanodiagnosis of carcinoembryonic antigen (CEA): an approach to classification and precise detection of cancer biomarker. Bionanoscience, 2024. **14**(1): p. 429-446.
18 .Yadav, G.K. and S.K. Metya, Plasmonic nanosensor for cancer cell detection with multi Fano resonance. Plasmonics, 2023. **18**(3): p. 1195-1202.
19 .Zhao, L. and C. Mao, Photoelectrochemical Immunosensor for Carcinoembryonic Antigen Detection: An Attempt for Early Cancer Screening, in Advances in Fabrication and Investigation of Nanomaterials for Industrial Applications. 2024, Springer. p. 91-109.
20 .Darabi, A. and M.R.J.S.R. Malekshahi, Design and optimization of a compact dual band metal insulator metal filter for high sensitivity refractive index sensing using particle swarm optimization. 2025. **15** (1): p. 22436.
21 .Wang, Y., et al., On-chip plasmonic nanosensor based on multiple Fano resonances in rectangular coupled systems. Optics Communications, 2023. **549**: p. 129915.
22 .Tasnim, N. and A.S. Mohsin, Nanohole array integrated metal insulator metal)MIM) based structure employing dual mode SPR sensor for detection of Hemoglobin (Hb) in blood. Heliyon, 2024. **10** (12).
23 .Yadav, G.K. and S.K.J.I.J.o.R. Metya, Multi fano resonance-based plasmonic MIM nanosensor for label-free virus detection. 2024. **70** (9):p. 7597-7606.
24 .Xingchun, Y., T. Jinping, and Y.J.O.-E.E. Rongcao, Transmission characteristics of a Y-shaped MIM plasmonic waveguide with side-coupled cavities. 2025. **44**(10): p. 1004-1013.
25 .Molaei-Yeznabad, A., et al., Numerical simulation plasmonic biosensor based on metal-insulator-metal waveguide for label-free and non-invasive detection of prostate-specific antigen. 2025: p. 100937.
26 .Berini, P., Long-range surface plasmon polaritons. Advances in optics and photonics, 2009. **1**(3): p. 484-588.
27 .Economou, E., Surface plasmons in thin films. Physical review, 1969. **182**(2): p. 539.
28 .Homola, J., Surface plasmon resonance sensors for detection of chemical and biological species. Chemical reviews, 2008. **108**(2): p. 462-493.
29 .Choi, E., et al ,.Highly sensitive tactile shear sensor using spatially digitized contact electrodes. Sensors, 2019. **19**(6): p. 1300.
30 .Bahador, H., Five-segment THz refractive index metamaterial biosensor with perfect absorption for carcinoembryonic antigen measurement .IEEE Sensors Journal, 2024.
31 .Jung, W.K. and K.M. Byun, Fabrication of nanoscale plasmonic structures and their applications to photonic devices and biosensors. Biomedical Engineering Letters, 2011. **1**: p. 153-162.

32 .Lee, S.-W., et al., Highly sensitive biosensing using arrays of plasmonic Au nanodisks realized by nanoimprint lithography. ACS nano, 2011. **5**(2): p. 897-904.
33 .Zhang, W. and S.Y. Chou, Multilevel nanoimprint lithography with submicron alignment over 4 in. Si wafers. Applied physics letters, 2001. **79**(6): p. 845-847.
34 .Giannone, D., et al. NIL fabrication of a polymer-based photonic sensor device in P3SENS project. in Organic Photonics V. 2012. SPIE.
35 .Gao, H., et al., Air cushion press for excellent uniformity, high yield, and fast nanoimprint across a 100 mm field. Nano Letters, 2006. **6**(11): p. 2438-2441.
36 .Rahad, R., et al., Plasmonic metal-insulator-metal (MIM) refractive index sensor for glucose level monitoring. Plasmonics, 2024. **19**(5): p. 2605-2614.
37 .Rahad, R., N. Hossain ,and A.J.P. Hossain, Enhanced alcohol detection using surface plasmon polariton dependent MIM plasmonic sensor. 2025. **20**(3): p. 1331-1340.
38 .Butt, M.A., N. Kazanskiy, and S. Khonina, Tapered waveguide mode converters for metal-insulator-metal waveguide plasmonic sensors. Measurement, 2023. **211**: p. 112601.
39 .Chen, J.-H., et al., A refractive index sensor based on the MIM waveguide with a semi-elliptical and a rectangular ring resonant cavity. Modern Physics Letters B, 2023. **37**(30): p. 2350141.
40 .Treena, T.T., M.A. Karim, and N.M.J.O.E. Munim, Plasmonic detection of microplastics and microorganisms using a circular-nanorod-coupled MIM sensor. 2026. **34**(10): p. 17692-17710.